



Iodine-Chemisorption, Interpenetration and Polycatenation: Cationic MOFs and CPs from Group 13 Metal Halides and Di-Pyridyl-Linkers

Thomas C. Schäfer,^[a] Jonathan Becker,^[a] Marcel T. Seuffert,^[a] Dominik Heuler,^[a]
Alexander E. Sedykh,^[a] and Klaus Müller-Buschbaum^{*[a, b]}

Dedicated to Prof. Dr. Holger Braunschweig on the occasion of his 60th birthday.

Abstract: Eight cationic, two-dimensional metal-organic frameworks (MOFs) were synthesized in reactions of the group 13 metal halides AlBr₃, AlI₃, GaBr₃, InBr₃ and InI₃ with the dipyridyl ligands 1,2-di(4-pyridyl)ethylene (*bpe*), 1,2-di(4-pyridyl)ethane (*bpa*) and 4,4'-bipyridine (*bipy*). Seven of them follow the general formula $^2_{\infty}[\text{MX}_2(\text{L})_2]\text{A}$, M=Al, In, X=Br, I, A[−]=[MX₄][−], I[−], I₃[−], L = *bipy*, *bpa*, *bpe*. Thereby, the porosity of the cationic frameworks can be utilized to take up the heavy molecule iodine in gas-phase chemisorption vital for the capture of iodine radioisotopes. This is achieved by switching between I[−] and the polyiodide I₃[−] in the cavities at room temperature, including single-crystal-to-single-crystal transformation. The MOFs are 2D networks that exhibit (4,4)-

topology in general or (6,3)-topology for $^2_{\infty}[(\text{GaBr}_2)_2(\text{bpa})_5][\text{GaBr}_4]_2\text{-bpa}$. The two-dimensional networks can either be arranged to an inclined interpenetration of the cationic two-dimensional networks, or to stacked networks without interpenetration. Interpenetration is accompanied by polycatenation. Due to the cationic character, the MOFs require the counter ions [MX₄][−], I[−] or I₃[−] counter ions in their pores. Whereas the [MX₄][−] ions are immobile, iodide allows for chemisorption. Furthermore, eight additional coordination polymers and complexes were identified and isolated that elaborate the reaction space of the herein reported syntheses.

Introduction

Coordination polymers (CP)^[1–4] and metal-organic frameworks (MOF)^[5–7] are actively investigated materials for more than two decades, as they possess a large variety of features and properties, such as porosity,^[8] luminescence,^[9] optical,^[10] and magnetic properties.^[11] Porosity renders MOFs suitable as potential adsorption/separation materials for hazardous substances.^[12] Their customizability in a structural and chemical sense allows for the design of substrate specific adsorption materials, like radioisotopes of iodine (¹²⁹I, ¹³¹I), which arise as


toxic waste in nuclear power plants. In the recent past, several reports focus on iodine capture using MOFs. The investigated systems can be divided into non-iodide containing and iodide containing MOFs, whereby iodine capture occurs via physi- or chemisorption.^[13] The latter was found *inter alia* for redox active MOFs by oxidizing the framework with I₂^[14] as well as for MOFs, possessing accessible iodide groups in its pores, which react with iodine under formation of polyiodides.^[15]


However, porosity requires an open network structure with accessible pores, which is contrary to the dense packing of solids and a minimum in energy. The latter is one of the controlling forces for the phenomenon of interpenetration^[16–23] of two or more entangled polymers.^[24] Other reasons for interpenetration reported are weak supramolecular interactions, such as van der Waals forces, H-bonding and π - π interactions,^[25] elongation of the organic linkers, occurring together with intercalation of template molecules, such as solvents and complex anions.^[26,27]

The incorporation of complex anions in the structures is found for cationic coordination polymers and MOFs including group 13 metal halide based compounds constituted together with N-donor ligands.^[28–38] Although being less frequent than carboxylate based MOFs and CPs,^[39–46] the research concerning N-donor based coordination polymers with group 13 metals has gained growing interest. Until now, only a limited amount of coordination polymers constituted from group 13 metal halides and N-donor ligands have been reported, for example

[a] T. C. Schäfer, J. Becker, M. T. Seuffert, D. Heuler, A. E. Sedykh,
Prof. Dr. K. Müller-Buschbaum
Institute of Inorganic and Analytical Chemistry
Justus-Liebig University Giessen
Heinrich-Buff-Ring 17, 35390 Giessen (Germany)
E-mail: kmbac@uni-giessen.de

[b] Prof. Dr. K. Müller-Buschbaum
Center for Materials Research (LaMa)
Justus-Liebig University Gießen
Heinrich-Buff-Ring 16, 35390 Giessen (Germany)

 Supporting information for this article is available on the WWW under
<https://doi.org/10.1002/chem.202104171>

 © 2022 The Authors. Chemistry - A European Journal published by Wiley-VCH GmbH. This is an open access article under the terms of the Creative Commons Attribution Non-Commercial License, which permits use, distribution and reproduction in any medium, provided the original work is properly cited and is not used for commercial purposes.

for the linkers pyrazine (*pyz*),^[28,34] 4,4'-bipyridine (*bipy*),^[31–33,37,38] 1,2-di(4-pyridyl)ethylene (*bpe*)^[29,35] and 2,4,6-tri(4-pyridyl)-1,3,5-triazine (*tpt*).^[30,36] Stability analysis of the bulk materials, such as simultaneous DTA/TG of phase pure CPs and MOFs were only rarely reported, for example for $^1_\infty[\text{GaCl}_3(\text{bpe})]$, $^2_\infty[\text{Ga}_2\text{Cl}_4(\text{bpe})_2]$, $^1_\infty[\text{GaCl}_2(\text{bpe})_2][\text{GaCl}_4]_4 \cdot 3\text{bpe}$ and $^1_\infty[\text{MX}_3(\text{tpt})]$ ($\text{MX}_3 = \text{AlBr}_3$, GaCl_3 , GaBr_3 and InI_3).^[35,36] A recent work reported on the single-crystal syntheses of the aluminum and gallium based CPs $^2_\infty[\text{M}_2\text{Cl}_4(\text{bpe})_2]$, $^1_\infty[\text{MCl}_2(\text{bpe})_2][\text{MCl}_4]_4 \cdot 3\text{bpe}$, the AlBr_3 based one-dimensional CP $^1_\infty[\text{Al}_3\text{Br}_8(\text{bpe})_3][\text{AlBr}_4]$ and the two-dimensional CP $^2_\infty[\text{Al}_2\text{Br}_4(\text{bpe})_2][\text{AlBr}_4]_2 \cdot \text{bpe}$.^[29,35] In this work, we present eight two-dimensional MOFs with and without interpenetration, which were investigated by SCXRD, PXRD, DTA/TG, IR-spectroscopy, elemental analysis as well as iodine chemisorption. Furthermore, we report on eight additional side phases of the reported reactions that range from one-dimensional coordination polymers down to monomeric complexes. All products can form in a rather narrow region of reaction parameters, which allows for the formation of several phases next to one another.

Results and Discussion

Crystal structures

The cationic one- and two-dimensional MOFs and CPs 1–9, as well as the cationic complex 10 are constituted from the group 13 metal halides AlBr_3 , AlI_3 , GaBr_3 , InBr_3 and InI_3 together with the ligands 4,4'-bipyridine (*bipy*), 1,2-di(4-pyridyl)ethylene (*bpe*) and 1,2-di(4-pyridyl)ethane (*bpa*). They contain metal centers in an octahedral coordination environment. Hereby, each M^{3+} is coordinated by two halido ligands in axial positions and four nitrogen atoms of the respective linker in equatorial positions. This results in cationic nodes, which are interconnected by the neutral linkers in one or two dimensions resulting in cationic strands or nets. Charge compensation is accomplished by MX_4^- , iodide or triiodide counter anions. 1–8 are open frameworks with tunnels extending through the crystal structures and thus can be considered as cationic MOFs since they contain potentially accessible voids. $^2_\infty[\text{AlI}_2(\text{bpe})_2]\text{I} \cdot \text{tol}$ (1) (*Pccn*), $^2_\infty[\text{AlI}_2(\text{bpa})_2][\text{AlI}_4]$ (2) (*I4c2*), $^2_\infty[\text{AlI}_2(\text{bpe})_2]\text{I}_3$ (3) (*P4/ncc*), $^2_\infty[\text{AlBr}_2(\text{bpe})_2][\text{AlBr}_4]$ (4) (*Pbcn*) and the three isotopic (*C2/c*) MOFs $^2_\infty[\text{MX}_2(\text{bipy})_2][\text{MX}_4]$ (MX_3 : AlI_3 , 5; InBr_3 , 6; InI_3 , 7) consist of uninodal 4-c nets (fourfold connectivity) with a (4,4)-net topology, as depicted in Figure 1 for 1 and 2 (also see Figures S1–4, Supporting Information).

Although 1–7 possess the same (4,4)-net topology, only 1–3 show an 2D→3D diagonal/diagonal inclined interpenetration. This means the overall entanglement is three-dimensional and formed by two-dimensional nets, where the mean planes in the interpenetrating layers are parallel. The inclined interpenetration occurs via rhombic (4,4)-nets, which are diagonally entangled, respectively (see Figure 2).^[47,48]

The case where interpenetration leads to higher dimensionalities than those of the discrete polymer from which the overall structure is formed, is also known as polycatenation.^[49] This is an extension of the definition of interpenetration, meaning

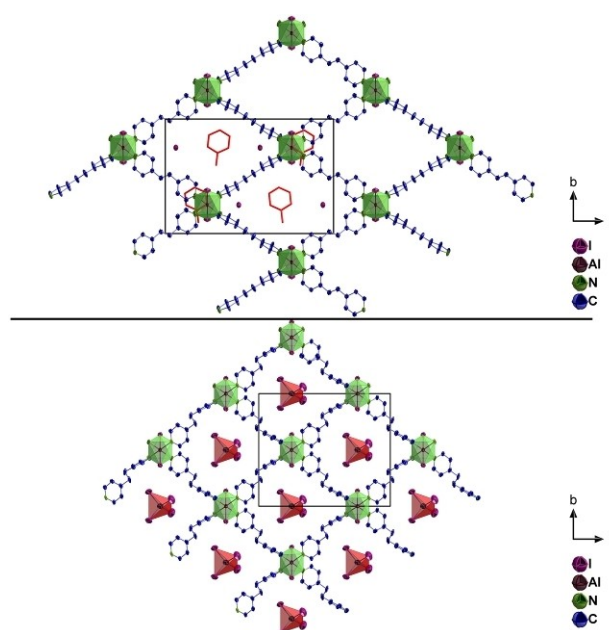


Figure 1. Excerpts of the crystal structures of $^2_\infty[\text{AlI}_2(\text{bpe})_2]\text{I} \cdot \text{tol}$ (1) (Top) and $^2_\infty[\text{AlI}_2(\text{bpa})_2][\text{AlI}_4]$ (2) (Bottom), both with a view along [100]. Polyhedra of the octahedrally coordinated Al^{3+} are depicted in green. For better clarity, only one cationic layer is depicted, incorporated toluene (Top) is depicted as wire and stick model and tetrahedrally coordinated $[\text{AlI}_4]^-$ is highlighted in red (Bottom). All hydrogen atoms are omitted and thermal ellipsoids shown at 50% probability.

there are two or more entangled polymers, which cannot be separated without the breaking of topological bonds.^[47]

Polycatenation is found for 1–3, where upon inclined interpenetration with interpenetration angles α of 77° (1) and 90° (2–3), diamond-shaped tunnels are formed, which are extending along the crystallographic *c*-axis. The resulting voids are additionally occupied by the complex counter anion, for example $[\text{AlI}_4]^-$ in 2. In comparison, the steric demand of iodide in 1 is much smaller and therefore additional toluene molecules are incorporated into the void space.

In order to investigate the potential porosity of MOF 1, a gas-phase sorption experiment on red single-crystals of 1 (orthorhombic, *Pccn*) with I_2 was carried out, resulting in black single-crystals of $^2_\infty[\text{AlI}_2(\text{bpe})_2]\text{I}_3$ (3) (tetragonal, *P4/ncc*) in a single-crystal to single-crystal transformation. A depiction of 3 is shown in Figure 3 (also see Figures S5–8, Supporting Information).

The SCXRD investigation reveals the formation of triiodide upon I_2 sorption, which is occupying the void space of 3. Thus, the formation of 3 occurs via a post-synthetic anion modification of 1 by I_2 , accompanied with the desorption of initially incorporated toluene. Both, I_3^- formation and the loss of toluene, triggers a rearrangement of the interpenetrating cationic layers, as the interpenetration angle α of 77° (1) changes to 90° (3). These structural changes lead to an increase of the symmetry of the crystal structure.

In contrast to 1–3, $^2_\infty[\text{AlBr}_2(\text{bpe})_2][\text{AlBr}_4]$ (4) and the three isotopic MOFs $^2_\infty[\text{AlI}_2(\text{bipy})_2][\text{AlI}_4]$ (5), $^2_\infty[\text{InBr}_2(\text{bipy})_2][\text{InBr}_4]$ (6),

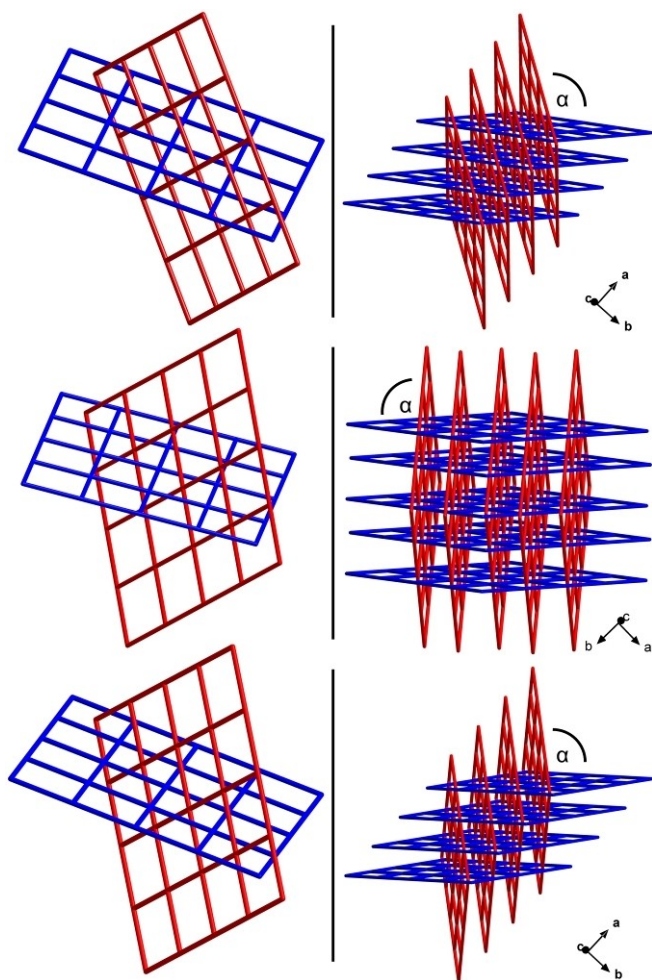


Figure 2. Topological representations of $^2_{\infty}[\text{Al}_2(\text{bpe})_2]\cdot\text{tol}$ (1) (Top, Left and Right), $^2_{\infty}[\text{Al}_2(\text{bpa})_2][\text{Al}_4]$ (2) (Center, Left and Right) and $^2_{\infty}[\text{Al}_2(\text{bpe})_2]_3$ (3) (Bottom, Left and Right). The three depictions on the left side show two interpenetrating (4,4)-nets. The depictions on the right side are topological representations, illustrating the inclined parallel interpenetration with interpenetration angles $\alpha = 77^\circ$ (1) and 90° (2–3).

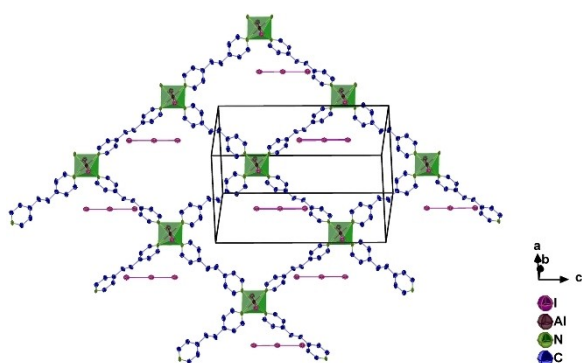


Figure 3. Excerpt of the crystal structure of $^2_{\infty}[\text{Al}_2(\text{bpe})_2]_3$ (3). The polyhedra of the octahedrally coordinated Al^{3+} are depicted in green. For better clarity, only one cationic layer is depicted. All hydrogen atoms are omitted and thermal ellipsoids shown at 25% probability.

$^2_{\infty}[\text{In}_2(\text{bipy})_2][\text{In}_4]$ (7) do not show interpenetration. A depiction of the crystal structure is shown in Figure 4 for 4 and 5 (also see Figures S9–16, Supporting Information). In comparison with the literature, the uninodal (4,4)-net topology is a common structural motif for group 13 metal based CPs and is reported for $^2_{\infty}[\text{AlBr}_2(\text{pyz})_2][\text{AlBr}_4]$, $^2_{\infty}[\text{MX}_2(\text{bipy})_2][\text{MX}_4]$ ($\text{MX}=\text{AlCl}$, AlBr , GaBr) and $^2_{\infty}[\text{GaCl}_2(\text{bipy})_2][\text{GaCl}_4]\cdot 2 \text{ bipy}$. These compounds show also no interpenetration, like 4–7.^[38] As already mentioned, a beneficial packing for the *pyz*- and *bipy*-based MOFs is achieved without interpenetration, whereas coordination compounds constructed from elongated linkers like *bpe* and *bpa* tend to interpenetrate. However, $^2_{\infty}[\text{AlBr}_2(\text{bpe})_2][\text{AlBr}_4]$ (4) is isorecticular to 5–7 with no interpenetration being observed. The reasons and controlling forces for this behaviour are not explicitly known. The latter include van-der-Waals forces, H-bonding and π - π interactions, which are the main interactions between the individual entangled networks. This further enables a certain structural flexibility of the structures, as it was observed in the single-crystal to single-crystal phase transformation from 1 to 3.^[25] The presence of interpenetration of

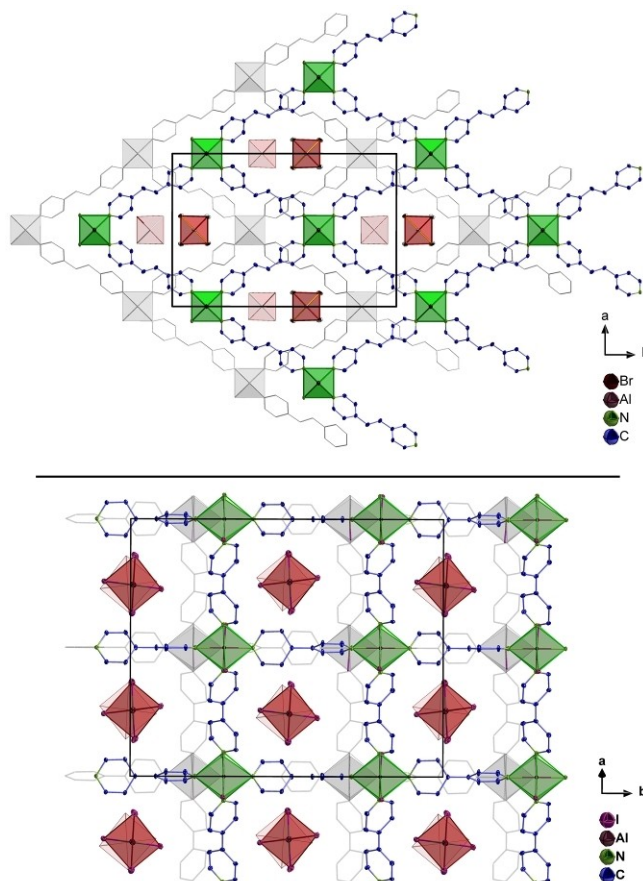


Figure 4. Crystal structures of $^2_{\infty}[\text{AlBr}_2(\text{bpe})_2][\text{AlBr}_4]$ (4) (Top) and $^2_{\infty}[\text{Al}_2(\text{bipy})_2][\text{Al}_4]$ (5) (Bottom) with a view along [001], highlighting the cationic two-dimensional nets. The corresponding $[\text{AlBr}_4]^-$ (4), $[\text{Al}_4]^-$ (5) counter anions are depicted in red and the Al^{3+} -centered octahedra of the cationic nets are depicted in green. For better clarity, the second cationic two-dimensional nets are greyed out. All hydrogen atoms are omitted and thermal ellipsoids shown at 50% probability.

the herein described 2D networks can be attributed to the different character of the counter anion $[\text{AlBr}_4]^-$ compared to I^- and $[\text{AlI}_4]^-$ in **1** and **2**, as well as to an energetically more beneficial packing with reduced voids. In addition, also intermolecular $\text{I}\cdots\text{H}$ interactions contribute to the found interpenetration of **1–3**. The shortest $\text{I}\cdots\text{H}$ contacts were determined as 318.0(3)–327.4(1) pm ($\text{I}^-\cdots\text{bpe}$) and 309.82(7) pm ($\{[\text{AlI}_2\text{N}_4]^{2+}\cdots\text{tol}\}$) for **1**, 332.49(9) pm ($[\text{AlI}_4]^- \cdots \text{bpa}$) for **2** and 330.6(1) pm ($\text{I}_3^- \cdots \text{bpe}$) for **3**. These values are in the same range as other intermolecular $\text{X}\cdots\text{H}$ contacts ($\text{X}=\text{Cl}, \text{Br}$, 290–310 pm) reported for group 13 metal halide and N-donor based CPs.^[29]

The MOFs **4–7** possess diamond-shaped cavities extending through the crystal structures, formed upon stacking of the cationic layers in a parallel fashion in an AB sequence along the crystallographic c -axis. The complex counter anions are incorporated into the resulting cavities.

The reaction of GaBr_3 with *bpa* leads to the formation of the cationic, two-dimensional MOF $^2_\infty[\text{GaBr}_2]_2(\text{bpa})_5[\text{GaBr}_4]_2\cdot\text{bpa}$ (**8**), which crystallizes in the monoclinic crystal system with the space group Pc . A depiction of the crystal structure is given in Figure 5 (also see Figures S17–18, Supporting Information). In **8**, each Ga^{3+} serves as node with a threefold connectivity (3-c) and is coordinated by two bromido ligands and four nitrogen atoms of *bpa* in an octahedral fashion. Thus, the cationic MOF **8** can be reduced to a (6,3)-net, with six gallium-centered 3-c

nodes, whereby the overall topology is a uninodal 3-c net with the point symbol (6^3) . The individual $^2_\infty[\text{GaBr}_2]_2(\text{bpa})_5^{2+}$ -layers of **8**, lying in the crystallographic a - b plane, are stacking parallel to each other in an AB sequence along the crystallographic c -axis. This results in a packing with tunnels extending through the crystal structure along $[001]$. Charge compensation is accomplished by corresponding $[\text{GaBr}_4]^-$ ions, which are incorporated in the voids of the open framework together with uncoordinated *bpa* ligand.

Compared to chemically related structures reported in the literature, the (6,3)-net topology, originating from octahedral coordinated M^{3+} serving as 3-c node, is, next to the (4,4)-topology, a common structural motif for group 13 metal halide based coordination polymers. It has previously been reported for the compounds $^2_\infty[\text{M}_2\text{X}_4(\text{bpe})_2]^{1+}[\text{MX}_2(\text{bpe})_3]_2[\text{MX}_4]_4\cdot 3\text{bpe}$ ($\text{M}=\text{Ga}, \text{Al}$, $\text{X}=\text{Cl}$), which contain neutral, one-dimensional chains and cationic nets as well as for CP $^2_\infty[(\text{AlBr}_2)_2(\text{bpe})_5][\text{AlBr}_4]\cdot\text{bpe}$.^[29,35]

During the research on **1–8**, we were also able to structurally characterize a larger number of other phases: another cationic but one-dimensional coordination polymer $^1_\infty[\text{AlI}_2(\text{bpe})_3]\cdot\text{bpe}$ (**9**) (triclinic, $P\bar{1}$), the cationic complex $[(\text{AlI}_2)_2(\text{bpe})_7]_2\cdot(\text{Hbpe})\text{I}$ (**10**) (triclinic, $P\bar{1}$) as well as a distinct amount of further dimeric complexes: $[(\text{AlBr}_3)_2(\text{bpe})]$ (**11**) (monoclinic, $P2_1/n$), $[(\text{AlI}_3)_2(\text{bpe})]$ (**12**) (monoclinic, $P2_1/n$), $[(\text{AlI}_3)_2(\text{bpa})]$ (**13**) (monoclinic, $P2_1/c$), $[(\text{GaBr}_3)_2(\text{bpa})]$ (**14**) (monoclinic, $P2_1/c$), $[(\text{AlI}_3)_2(\text{bipy})]\cdot 0.5 \text{ tol}$ (**15**) (orthorhombic, $Pbca$) and $[(\text{GaBr}_3)_2(\text{bipy})]\cdot 0.5 \text{ tol}$ (**16**) (orthorhombic, $Pbca$). A depiction of the cationic CP **9**, complex **10** as well as of the binuclear complexes **11–16** on the basis of $[(\text{AlI}_3)_2(\text{bpe})]$ (**12**) is given in Figure 6 (also see Figures S19–27, Supporting Information).

In its crystal structure, **9** is constituted by octahedrally coordinated Al^{3+} , with the metal center being axially coordinated by two iodido ligands and equatorially by four nitrogen atoms of *bpe*. The Al^{3+} -centered octahedra serve as nodes with a twofold connectivity, interconnected by *bpe* to one-dimensional chains. Hereby the individual chains extend along the crystallographic b -axis, with *bpe* being incorporated in the crystal structure. The remaining two *bpe* ligands of every node are uncoordinated. Charge compensation of the cationic CP is accomplished by iodide, alike **1**.

In comparison to **9**, the molecular, binuclear cationic complex $[(\text{AlI}_2)_2(\text{bpe})_7]_2\cdot(\text{Hbpe})\text{I}$ (**10**) is structurally closely related, exhibiting identical Al^{3+} -centered octahedra. Two Al^{3+} -centered nodes are interconnected by *bpe*, forming the complex $[(\text{AlI}_2)_2(\text{bpe})_7]^{2+}$ with iodide as counter anion. The remaining three *bpe* ligands of each octahedron are uncoordinated. Next to the cationic complexes, the crystal structure of **10** contains another equivalent of I^- counterions and the protonated ligand Hbpe^+ . Except for the missing extension of the Al^{3+} -nodes to a one-dimensional chain or to a two-dimensional network by *bpe*, the structural motif of **10** is closely related to the structural motifs found for MOF **1** and CP **9**. They also coincide with **10** in the charge compensation being accomplished by iodide.

Altogether, the structural motif of an octahedrally coordinated $[\text{AlI}_2]^+$ by four N-donor ligands has, to the best of our

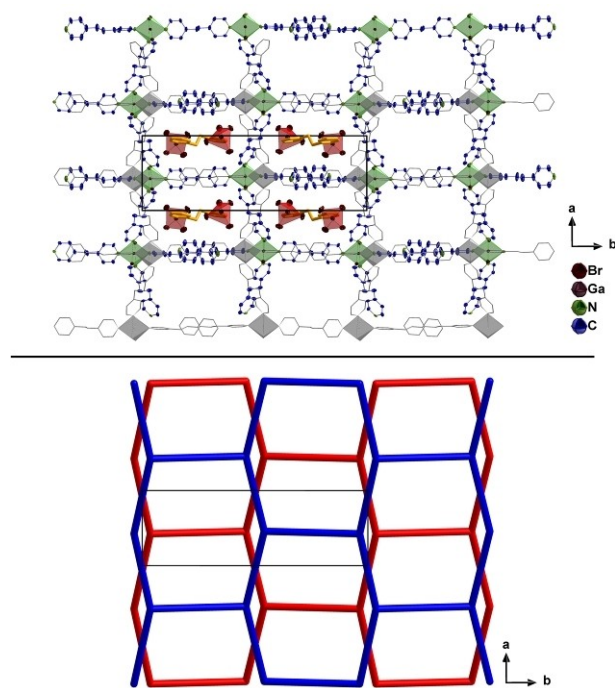


Figure 5. Crystal structure of $^2_\infty[\text{GaBr}_2]_2(\text{bpa})_5[\text{GaBr}_4]_2\cdot\text{bpa}$ (**8**) with a view along $[001]$ highlighting one two-dimensional $^2_\infty[\text{GaBr}_2]_2(\text{bpa})_5^{2+}$ -net (Top). Corresponding $[\text{GaBr}_4]^-$ counter anions are depicted in red. The Ga^{3+} -centered octahedra of the cationic net are depicted in green. Incorporated *bpa* is highlighted in orange as wire and stick model. For better clarity, the second $^2_\infty[\text{GaBr}_2]_2(\text{bpa})_5^{2+}$ -net is greyed out. All hydrogen atoms are omitted and thermal ellipsoids shown at 50% probability. Topological representation of **8** as uninodal 3-c nets, with a (6,3)-net topology (Bottom). The individual layers are stacking in an AB sequence parallel to each other along $[001]$.

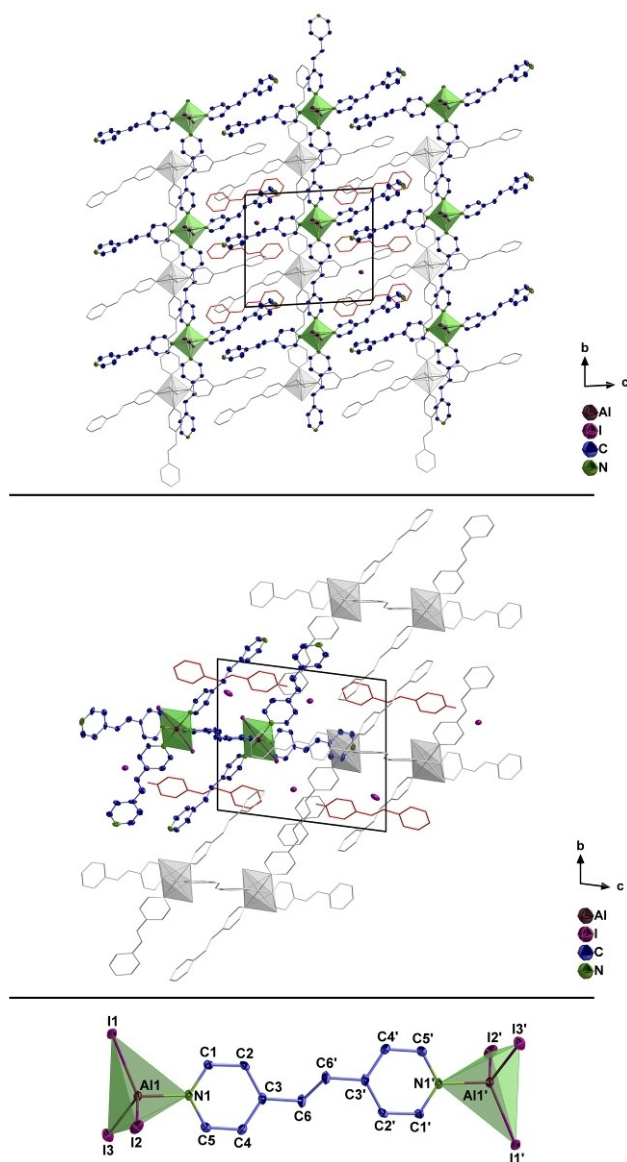


Figure 6. Crystal structures of $[\text{AlI}_2(\text{bpe})_3]\text{I} \cdot \text{bpe}$ (**9**) (Top) and $[(\text{AlI}_2(\text{bpe})_7)\text{I}_2] \cdot (\text{Hbpe})\text{I}$ (**10**) (Center) with a view along [100] as well as coordination of *bpe* to two Al^{3+} ions in the complex $[(\text{AlI}_2(\text{bpe})_7)\text{I}_2]$ (**12**) (Bottom). The polyhedra of octahedrally and tetrahedrally coordinated Al^{3+} ions are depicted in green. Incorporated, non-coordinating *bpe* and $(\text{Hbpe})^+$ are depicted in red as wire and sticks. For better clarity, selected parts within the unit cells are greyed out and all hydrogen atoms are omitted. Thermal ellipsoids shown at 50% probability. Symmetry operation: $I = -x, -y, -z$.

knowledge, not been reported yet. Therefore a comparison of the interatomic distances for **1**, **2**, **3**, **5**, **9** and **10** has to be drawn with other compounds, such as the complex $[\text{AlI}_3(\text{tmpH})]$ with 2,2,6,6-tetramethylpiperidine as N-donor ligand.^[50] The ligands *bpe* and *bpa* in **1** and **2** were found to be disordered and were refined with the help of restraints. An influence on the interatomic distances has to be considered for the discussion and the related comparison with the literature. The interatomic distances for the herein described cationic compounds **1**, **2**, **3**, **5**, **9** and **10** are in good accordance to one another and were determined to be between 274.0(1)–278.5(2) pm for Al–I and

202.2(3)–207.8(3) pm for Al–N (also see Tables S8–10, S12, S16–17, Supporting Information). Compared to the complex $[\text{AlI}_3(\text{tmpH})]$ (Al–I: 253.2–254.0 pm; Al–N: 203.8 pm),^[50] where Al^{3+} is coordinated by three iodo ligands and one N-donor ligand in a tetrahedral fashion, the interatomic Al–N distances match well, whereas the Al–I distances are elongated by 20 pm. This behavior is attributed to the increase in coordination number (CN) from four to six. Compound **4** exhibits interatomic distances for the $\{\text{AlBr}_2\text{N}_4\}^+$ nodes for Al–Br of 247.8(1) pm and 204.7(2)–206.8(2) pm for Al–N, whereas the interatomic distances for the corresponding $[\text{AlBr}_4]^-$ counter anions are 229.0(1)–230.2(1) pm (also see Table S11, Supporting Information). These values are in an expected range, compared to chemical and structural related compounds, such as $^2_\infty[(\text{AlBr}_2)_2(\text{bpe})_5][\text{AlBr}_4]_2 \cdot \text{bpe}$ (Al–Br: 247.2–247.8 pm, Al–N: 202.8–207.5 pm), reported in the literature.^[29] **8** possesses interatomic Ga–Br distances of 246.7(1)–251.1(1) pm and Ga–N distances of 208.0(9)–213.2(6) pm, which are close to values, reported for example for the cationic, molecular complex $[(\text{GaBr}_2)_2(\text{bpe})_7][\text{GaBr}_4]$ (Ga–Br = 248.8 pm and 251.9 pm; Ga–N = 209.3–211.6 pm) (also see Table S15, Supporting Information).^[29] A comparison of the interatomic distances determined by SCXRD of **6** and **7** to one another, reveals good agreement of the In–N distances, which are 226.8(4)–228.6(6) pm for **6** and 229.6(4)–230.3(4) pm for **7**. In contrast, the In–X distances differ by 20 pm (MOF **6**, In–Br: 259.5(1)–260.2(1) pm; MOF **7**, In–I: 280.5(1)–281.2(1) pm), as expected (also see Tables S13–14, Supporting Information). A comparison can be drawn with complexes, such as $[\text{InBr}_3(\text{py})_3]$ ^[51] (In–N: 228–231 pm; In–Br: 259.3–261.8 pm) and $[\text{InI}_3(\text{py})_3]$ ^[52] (In–N: 230.9–232.3 pm; In–I: 283.9–286.7 pm) (*py* = pyridine), revealing a good agreement concerning the In–N– and In–X (X = Br, I) distances. In contrast to **1**–**10**, the central M^{3+} of the neutral complexes **11**–**16** is coordinated by three halido ligands and one nitrogen atom of the respective linker in a tetrahedral fashion. Therefore, the coordination number (CN) is decreased from six to four, compared to **1**–**10**, affecting a shortening of the interatomic M–X distances of **11**–**16** ($\Delta_{\text{Al-Br}} = 20$ pm; $\Delta_{\text{Al-I}} = 25$ pm; $\Delta_{\text{Ga-Br}} = 20$ pm) (also see Tables S18–23, Supporting Information). The found interatomic distances are: 193.5(3) pm (Al–N) and 227.0(1)–227.3(1) pm (Al–Br) for **11**; 193.7(3)–195.8(2) pm (Al–N) and 248.8(2)–252.9(1) pm (Al–I) for **12**, **13**, **15**; 198.5(3) pm–199.9(3) pm (Ga–N) and 227.9(1)–231.7(1) pm for **14** and **16**. These values match well with compounds based on AlBr_3 , AlI_3 , GaBr_3 with N-donor ligands exhibiting a tetrahedrally coordinated M^{3+} central atom, such as $[\text{AlBr}_3(\text{py})_3]$,^[37] $[(\text{AlBr}_3)_2(\text{L})]$ (L: *pyz*, *bipy*, *bpe*),^[29,38] $[\text{GaBr}_3(\text{py})_3]$,^[37] $[(\text{GaBr}_3)_2(\text{L})]$ (L: *pyz*, *bipy*, *bpe*),^[29,38] $[(\text{GaBr}_3)_2\text{bpe}] \cdot \text{bpe}$ and $[\text{AlI}_3(\text{tmpH})]$.^[29,50] For these literature known complexes, the interatomic distances are reported as: 224.6–229.5 pm for Al–Br and 193.5–199.9 pm for Al–N; 253.2–254.0 pm for Al–I and 203.9 pm for Al–N; 229.5–232.3 pm for Ga–Br and 197.9–200.0 pm for Ga–N.

Chemisorption of iodine

Due to the cationic character of the MOFs enforcing counter anions, also options to exchange and modify them post-synthetically were conducted. Whereas the $[MX_4]^-$ proved non-replaceable, size and positioning of the I^- ion in the pores renders it more suitable for modification. Although the heavy iodide itself could not be moved, it can be utilized as a reactivity spot for a chemisorption of iodine vapor. The radioactive isotopes of iodine, ^{129}I and ^{131}I are harmful fission products in nuclear power plants.^[53] If accidentally exposed to the environment, these isotopes have dangerous long-term impacts to the eco system and, owing to the active involvement in metabolic processes, to human health.^[54] This renders an effective capture of the highly volatile iodine isotopes via the gas phase highly important and a topic of great significance, for example in case of unwanted hazardous exposure of these

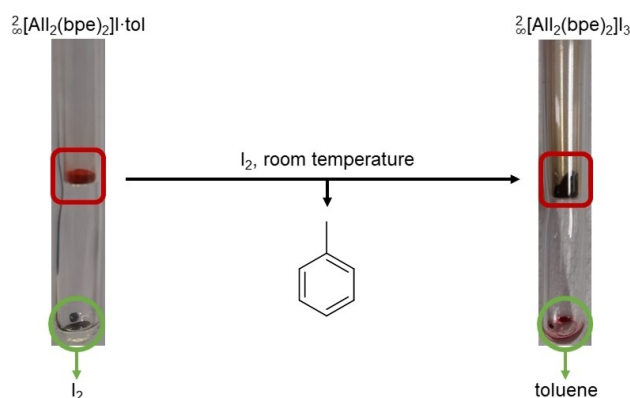


Figure 7. Depiction of the I_2 chemisorption experiment. Single-crystalline bulk material of **1** is placed separated from solid iodine.

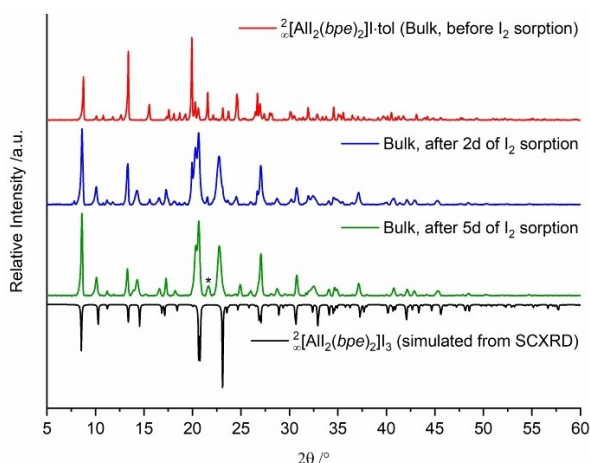


Figure 8. PXRD investigation of the post synthetic modification of MOF **1** by chemisorption of I_2 under formation of $2-[AlI_2(bpe)_2]I_3$ (**3**). The picture illustrates the diffraction pattern of **1** before (Red, Top), after 2 days (Blue, Top, Center) and after 5 days (Green, Bottom, Center) of I_2 uptake. The simulated diffraction pattern of **3** is given in black (Bottom). The reflection at 21.6° in 2θ of an unknown phase after the post-synthetic modification is marked with an asterisk.

isotopes.^[55] Benefitting from the porosity of the herein described MOF **1**, a gas phase sorption experiment at room temperature with iodine was carried out, leading to the formation of $2-[AlI_2(bpe)_2]I_3$ (**3**). Therefore, single-crystals of **1** were placed separately from solid iodine in an ampoule, which was sealed under reduced pressure ($p=1.0\times 10^{-3}$ mbar). A depiction, illustrating the sorption experiment, is given in Figure 7 and Figure S43, Supporting Information.

During this experiment, the initially red color of **1** changes within minutes to black upon reaction of iodine vapor with the iodide anion of **1** under formation of triiodide anions. This reaction is accompanied by the removal of incorporated toluene. Upon completion, investigations concerning the I_2 sorption by PXRD reveals complete reaction after 5 days in the sealed glass body under reduced pressure ($p=1.0\times 10^{-3}$ mbar) resulting in an uptake of one equivalent of I_2 per formula unit, as depicted in Figure 8. The resulting black color upon reaction with the iodine vapour underlines the formation of **3**. The formerly incorporated toluene accumulates at the bottom and can be observed as red liquid, since I_2 is partially dissolved. It is noteworthy, that the crystal shape does not change upon the I_2 sorption, since both, the bulk material before and after the treatment consists of needles and blocks of a similar size. The crystallinity does change however, as the obtained single-crystals diffract rather poorly with respect to the initial single-crystals of **1**. This also affects the PXRD measurement and leads to broadened reflections. Regardless of these issues, the resulting PXRD pattern of **3** shows good accordance to the powder pattern, simulated from SCXRD of **3** and except for one reflection at 21.6° in 2θ , no other reflections hinting to the presence of side phases are observed.

Investigations of the obtained bulk material of **3** by IR-spectroscopy reveals two $\nu(C=N)$ ring vibration modes at 1608 cm^{-1} and 1592 cm^{-1} hinting to the presence of two different phases in the sample. In comparison, these vibration bands do not originate from the precursor **1** ($\nu(C=N)=1613\text{ cm}^{-1}$) or the free ligand bpe ($\nu(C=N)=1594\text{ cm}^{-1}$). In general, linear I_3^- anions are IR active and the three IR-bands for symmetrical and asymmetrical stretching can be expected at approximately 110 cm^{-1} , $50\text{--}70\text{ cm}^{-1}$, and $130\text{--}140\text{ cm}^{-1}$.^[56]

As the iodine sorption experiments could not be carried out on a typical physi- or chemisorption analyzer, also the investigation of the desorption of iodine from **3** had to be investigated by a different set up. Therefore, the bulk material of **3** was investigated by DTA/TG in combination with mass spectrometry, which indicates a loss of iodine ($m/z=254$ and the MS fragmentation product iodine atoms ($m/z=127$)) at temperatures above 155°C in one step prior to the decomposition of the MOF at 245°C (see Figure 9 and Supporting Information, Figure S48). The remaining sample mass at 245°C is $\sim 76\%$ according the TG measurement and corresponds with the full desorption of I_2 ($\Delta m_{\text{calc}}=24.7\%$).

This shows that the iodine content can be desorbed at temperatures way below the decomposition temperature of the MOF.

Altogether, the iodine chemisorption under formation of $2-[AlI_2(bpe)_2]I_3$ (**3**) necessitates an open framework and accessi-

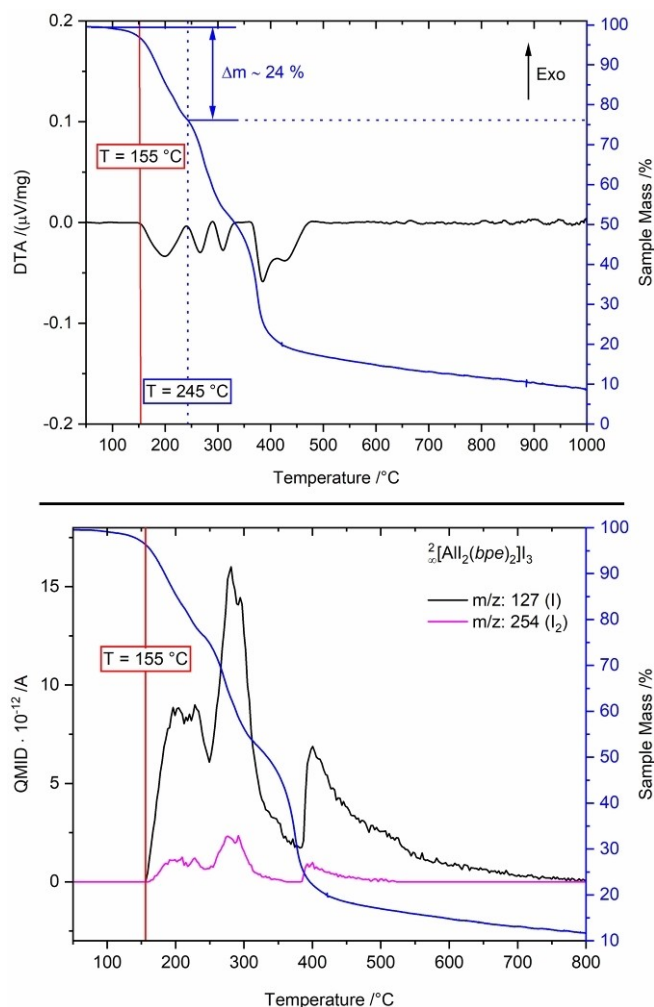


Figure 9. Simultaneous DTA/TG (Top) and mass spectrometry (Bottom) of **3**. The measurement was performed in a constant argon flow of $50 \text{ mL} \cdot \text{min}^{-1}$ with a heating rate of $5 \text{ K} \cdot \text{min}^{-1}$ from room temperature to 1000°C .

bility of the voids of $^2_\infty[\text{AlI}_2(\text{bpe})_2]\cdot\text{tol}$ (**1**). Its driving force is the reaction of I_2 with the iodide anion of **1** under formation of the triiodide anion and the loss of toluene. Related remarkable reactivity has been reported for $^3_\infty[\text{Cu}_4\text{I}_3(\text{DABCO})_2]\text{I}_3$ ($\text{DABCO} = \text{N,N-dimethyl-1,4-diazabicyclo[2.2.2]octane}$), with I_2 and I^- being located in its channels. Alike other copper halide based MOFs, this compound possesses also photoluminescence properties besides suitable porosity,^[57] allowing for additionally sensing of the reversible iodine uptake.^[58] Sensing of iodine in the gas phase is therefore one specialized application in the wide field of MOF chemistry, exemplified by various scientific studies reporting on luminescent MOFs and their capability as chemical and biological sensors.^[59] Another interesting process was reported for $^3_\infty[(\text{ZnI}_2)_3(\text{tpt})_2]$ ($\text{tpt} = 2,4,6\text{-tris(4-pyridyl)-1,3,5-triazine}$), where iodides of the Zn-centered nodes react with I_2 under formation of coordinated I_3^- .^[15] To the best of our knowledge, **1** marks the first example of a group 13 based MOF, allowing for a defined and stoichiometric I_2 chemisorption under formation of linear I_3^- , located in its cavities. In addition,

the herein described reaction to obtain **3** can be regarded as a single-crystal to single-crystal transformation in consideration of the structural changes discussed above.

Synthesis and stability

Reactions of group 13 metal halides of the heavy halides Br and I together with the linear N-donor ligands *bpa*, *bpe* and *bipy* lead to a large number of possible products within a rather narrow set of reaction parameters. Therefore, synthesis of the herein reported MOFs **1–2**, **4–5** and **7–8** with good phase purity for bulk analysis is challenging, since the formation of a specific reaction product based on group 13 metal halides and N-donor ligands is strongly dependent on the initial MX_3 to ligand ratio, as well as on the used reaction conditions. The used metal halides form complexes with Lewis basic solvents, such as pyridine, dmf or even acetonitrile, instead of coordination to the pyridyl-based N-donor ligands. Therefore, the herein described syntheses were performed in non-coordinative solvents, such as benzene, toluene, *m*-xylene and even liquid naphthalene. However, naphthalene is not fully suitable, as it decomposes in the presence of group 13 metal halides like AlI_3 at elevated temperatures under formation of insoluble decomposition products. Moreover, utilizing solvents in combination with group 13 metal halides necessitates ultra-dry solvents, especially if AlI_3 is employed together with N-donor ligands.

In contrast, the solvent-free melt synthesis, which is also used for the synthesis of MOFs and CPs,^[60] is beneficial concerning the water issue. However, a melt synthesis where the ligand serves as reactant and as liquid phase/solvent is limited to the self-consuming melt approach, since product formation is strongly dependent on the initial ligand to metal halide ratio. Therefore, reactions in a melt with excess ligand would lead to other unwanted reaction products with higher ligand contents. In addition, the self-consuming melt approach is also inhomogeneous with respect to a solvothermal approach,^[61] provided that the formed reaction products are solids without a melting point below the decomposition temperature. Nevertheless, this method has been successfully used for the synthesis of phase pure $^2_\infty[(\text{AlI}_2)_2(\text{bipy})_2][\text{AlI}_4]$ (**5**) and $^2_\infty[(\text{GaBr}_2)_2(\text{bpa})_3][\text{GaBr}_4]_2\cdot\text{bpa}$ (**8**), whereas the solvothermal approach is suitable for the bulk synthesis of $^2_\infty[\text{AlBr}_2(\text{bpe})_2][\text{AlBr}_4]$ (**4**) and $^2_\infty[\text{InI}_2(\text{bipy})_2][\text{InI}_4]$ (**7**). However, all attempts to develop a synthetic strategy for the synthesis of $^2_\infty[\text{InBr}_2(\text{bipy})_2][\text{InBr}_4]$ (**6**) with a fair phase purity failed. A depiction of the resulting powder pattern is given in Figure S28 in the Supporting Information.

Some of the herein reported synthetic procedures are non-standard and the syntheses of MOFs **1** and **2** differ significantly. The synthesis of $^2_\infty[\text{AlI}_2(\text{bpe})_2]\cdot\text{tol}$ (**1**) is achieved under solvothermal conditions with toluene as solvent under stirring at 225°C , whereas a self-consuming melt approach appeared not to be suitable for the synthesis of **1**. This is attributed to the absence of toluene in the melt approach, which is incorporated into the crystal structure of **1**. However, the herein described procedure for the synthesis of **1**, constituting AlI_3 with *bpe*

under solvothermal conditions, leads to a reaction product containing side phases, such as the complexes $[(\text{AlI}_2)_2(\text{bpe})_7]\text{I}_2 \cdot (\text{Hbpe})\text{I}$ (**10**) and $[(\text{AlI}_3)_2(\text{bpe})]$ (**12**). Therefore, an extensive washing procedure was carried out, to obtain **1** with a fair phase purity for further bulk analysis. The washing procedure consists of two steps, both carried out in sealed ampoules. complex **10** is removed from **1** by recrystallization above the solvent level. This separation is accomplished upon annealing at 225 °C without stirring. Better soluble side-phases, like complex **12**, are subsequently separated from **1** together with the solvent by decanting under solvothermal conditions in a closed system at 180 °C. The formation of complex **10**, which contains the hydrogen iodide adduct of *bpe* (*Hbpe*)I, further indicates the hydrolysis of AlI_3 under formation of hydrogen iodide even by traces of water inside the used solvent (20 ppm) and further hints to a catalytic pyrolyzation of the pyridine based linkers.^[62]

Investigations of the purified product **1** by PXRD show no reflections of possible crystalline side phases, whereas elemental analysis reveal a deviation in the theoretical and experimental carbon content (also see Figures S29, Supporting Information). The carbon content was found to be 2.7% lower than the theoretical value (Theoretical: C: 43.08 %, H: 3.27 %, N: 6.48 %; Found: C: 40.36 %, H: 3.02 %, N: 6.42 %), most likely caused by the presence of amorphous impurities. The significant number of side phases that are formed in low amounts, as reported herein for eight identified compounds **9–16**, show that multiple phases are stable within a close range of reaction conditions. The absence of observable side phases in PXRD indicates that they can be expected to be present in low amounts <5% or to be amorphous. Also changes in homogeneity and concentration gradients show an impact on product formation, resulting in the formation of single-crystals, characterized by SCXRD as **1**, **9** and **10**, within this product mixture. This substantiates the assumption that the reaction of AlI_3 with *bpe* under the herein reported conditions does not end in only one reaction product but in a mixture of stable compounds together with **1** as main product.

In contrast to **1**, ${}^{2}_{\infty}[\text{AlI}_2(\text{bpa})_2][\text{AlI}_4]$ (**2**) was successfully synthesized as phase pure bulk material. The synthesis combines both, self-consuming melt- and solvothermal approach. The initial reaction of AlI_3 with *bpa* under the herein

reported melt conditions leads to a reaction mixture with **2** as main product. Pure **2** can be obtained from the crude product in naphthalene at 270 °C and recrystallization upon cooling to 200 °C. In contrast, direct reaction under solvothermal conditions with naphthalene leads to an AlI_3 -catalyzed decomposition of the solvent.

The bulk materials of the syntheses of **1**, **2**, **4**, **5** and **7–8** were also investigated by powder x-ray diffraction experiments to gather information on the phase purity or possible side phases of the main products. Since the resulting diffraction patterns (298 K) and the powder patterns simulated from SCXRD data (100 K) are recorded at different temperatures, a direct comparison of reflections in terms of exact positions and intensities is difficult, as the reflection positions are temperature dependent. Therefore, Pawley fits were carried out, considering the thermal impact on the unit cell volumes of **1**, **2**, **4**, **5** and **7–8**. Representative depictions of the diffraction patterns and the corresponding Pawley fits of **1**, **2** and **7** are given in Figure 10 (also see Figures S29–37, Supporting Information).

The obtained Pawley fits for **1**, **2**, **4**, **5** and **8**, show no significant differences from the experimental data and are proof for a good crystallographic phase purity, whereas the resulting difference plot for **7** indicates the presence of negligible amounts of crystalline side phases. Furthermore, elemental analysis of **2**, **4**, **5** and **7–8** reveal no considerable deviation in the theoretical and experimental C–, H–, N– values and further proof the phase purity.

In addition, **1**, **2**, **4**, **5** and **7–8** were investigated by IR-spectroscopy to determine a successful coordination of the ligands *bipy*, *bpe* and *bpa* to the respective metal halides. This was accomplished by examination of the respective $\nu^-(\text{C}=\text{N})$ ring vibration modes at 1587 cm^{-1} (*bipy*), 1594 cm^{-1} (*bpe*) and 1593 cm^{-1} (*bpa*) of the free ligands. Coordination to a Lewis acid causes a hypsochromic shift of the $\nu^-(\text{C}=\text{N})$ ring vibration mode, as it lowers the aromatic conjugation within the pyridyl ring and therefore stabilizes the C=N bond.^[36] This shift was observed for all bulk materials, for which the $\nu^-(\text{C}=\text{N})$ ring vibration modes are shifted to 1613 cm^{-1} (**1**, $\Delta\nu^-(\text{C}=\text{N}) = 19 \text{ cm}^{-1}$), 1632 cm^{-1} and 1597 cm^{-1} (**2**, $\Delta\nu^-(\text{C}=\text{N}) = 39 \text{ cm}^{-1}$ and 3 cm^{-1}), 1617 cm^{-1} (**4**, $\Delta\nu^-(\text{C}=\text{N}) = 23 \text{ cm}^{-1}$), 1613 cm^{-1} (**5**, $\Delta\nu^-(\text{C}=\text{N}) = 26 \text{ cm}^{-1}$), 1607 cm^{-1} (**7**, $\Delta\nu^-(\text{C}=\text{N}) = 20 \text{ cm}^{-1}$) and 1619 cm^{-1} (**8**, $\Delta\nu^-(\text{C}=\text{N}) = 25 \text{ cm}^{-1}$) respectively. Additionally,

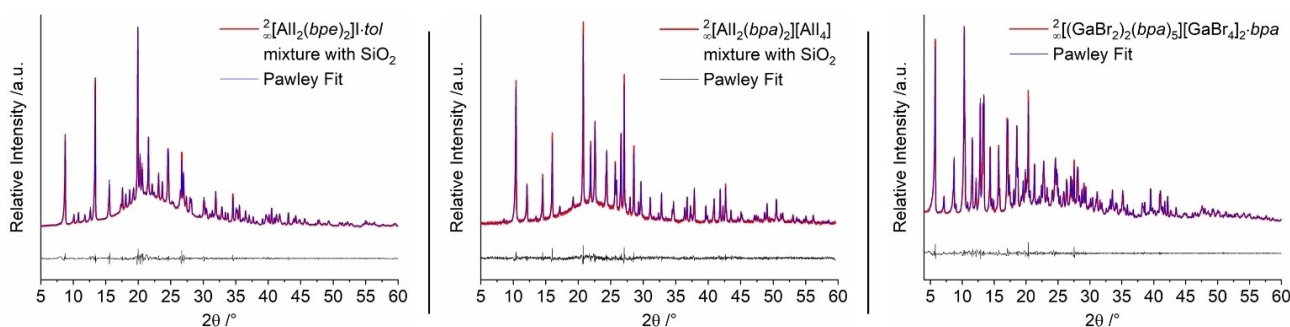


Figure 10. Evaluated PXRD data of **1** (Left), **2** (Middle) and **8** (Right), showing the experimental powder-X-ray diffraction data (Red) together with the calculated Pawley fits (Blue) as well as the corresponding difference plots (Black). ($\text{Cu-K}_{\alpha 1} = 154.1 \text{ pm}$).

the IR-spectrum of $^2_{\infty}[\text{GaBr}_2(\text{bpa})_3][\text{GaBr}_4]_2 \cdot \text{bpa}$ (**8**) shows the $\nu(\text{C}=\text{N})$ ring vibration mode of incorporated, uncoordinated *bpa* at 1599 cm^{-1} (also see Figures S38–42, Supporting Information).

Bulk materials of **1**, **2**, **4**, **5**, **7** were also investigated via simultaneous DTA/TG analysis to determine the thermal properties and stability of the compounds, as depicted in Figure 11. Evaluation of the obtained data reveals complex multi-step decomposition temperatures for the cationic MOFs **1**, **2**, **4** with onset temperatures of 275°C (**1**), 290°C (**2**) and 285°C (**4**) for the first steps. In comparison, **5** and **7** show higher thermal stabilities with decomposition temperatures of 310°C (**5**) and 360°C (**7**), whereby the endothermic signal of **7** with an onset temperature of 360°C depicts the beginning of two consecutive endothermic processes.

In spite of the volatility of the equivalent of intercalated toluene of **1** at temperatures below the first endothermic DTA-signal, the decomposition temperatures of **1**, **2**, **4**, **5**, **7** depict the beginning of ongoing, complex mass losses, with no distinct products being identifiable. The thermally least stable MOF **8** shows two consecutive endothermic phase transitions with onset temperatures of 140°C and 160°C with no correlating mass loss. According to the herein described synthetic procedure, where recrystallization of **8** from a self-consuming melt was observed upon cooling from 190°C to room temperature, these endothermic processes can be correlated with reversible phase transitions of **8**. This finding was further confirmed by a DSC measurement, where five cycles

of cooling and heating in a temperature range from 40°C to 240°C were carried out (also see Figure S47, Supporting Information).

Hereby, the two consecutive endothermic processes with onset temperatures of 140°C and 160°C were reproduced upon heating in all five cycles. To support this finding elucidated by the DSC measurement, the obtained colorless bulk material was additionally investigated by SCXRD, revealing the recrystallization of **8** out of the melt. Concerning the DTA/TG analysis of **8**, the melt is stable up to temperatures of almost 300°C . Above this temperature, decomposition and a significant mass loss start. Comparison of the thermal properties of **8** to the chemically related coordination polymer $^2_{\infty}[\text{Ga}_2\text{Cl}_4(\text{bpe})_5]_1[\text{GaCl}_2(\text{bpe})_3]_2 \cdot 3\text{bpe}$, reveals an initial mass loss at 200°C for the latter.^[35]

Conclusion

Eight cationic and two-dimensional MOFs with and without interpenetration based on the group 13 metal halides AlBr_3 , AlI_3 , GaBr_3 , InBr_3 , and InI_3 together with the bidentate dipyriddy ligands 4,4'-bipyridine (*bipy*), 1,2-di(4-pyridyl)ethylene (*bpe*) and 1,2-di(4-pyridyl)ethane (*bpa*) have been successfully synthesized. Charge compensation is achieved by $[\text{MX}_4]^-$ or X^- anions intercalated into the pores of the networks. They follow the general formula $^2_{\infty}[\text{MX}_2(\text{L})_2]\text{A}$, $\text{M}=\text{Al}$, In , $\text{X}=\text{Br}$, I , $\text{A}^-=[\text{MX}_4]^-$, I^- , I_3^- , $\text{L}=\text{bipy}$, *bpa*, *bpe*, whereas one has the formula $^2_{\infty}[(\text{GaBr}_2(\text{bpa})_3)_5][\text{GaBr}_4]_2 \cdot \text{bpa}$.

$^2_{\infty}[\text{AlI}_2(\text{bpe})_2]\text{I} \cdot \text{tol}$ is a remarkable example for iodine chemisorption and thus a potential sorption material for the radioisotopes of iodine, such as ^{129}I and ^{131}I , required for their uptake after unwanted, hazardous exposure to the environment. The MOF can take up one equivalent of iodine per formula unit by reversible formation of the polyiodide anion I_3^- at room temperature via the gas phase in a chemisorption process that was proven also for single-crystal-to-single-crystal transformation to $^2_{\infty}[\text{AlI}_2(\text{bpe})_2]\text{I}_3$. Desorption occurs at elevated temperatures below the decomposition temperature of the MOF. This underlines the versatility of cationic MOFs with intercalated anions, such as iodide, as they can act as reactivity centers for controlled gas phase chemisorption. Several of the presented MOFs exhibit an open framework structure with a (4,4)-topology and show an inclined interpenetration of the discrete cationic nets including polycatenation, into which iodide ions, $[\text{MX}_4]^-$ units, I_3^- , and toluene are incorporated. Interpenetration is favorable for the combination of the smallest M^{3+} cation Al^{3+} together with the largest $\text{X}^- = \text{I}^-$. The MOFs are accessible by a variety of different synthesis methods ranging from solvothermal to self-consuming melt reactions, which gave access also to several other coordination polymers and complexes in lower yield, which show that the stability of multiple phases overlaps depending on the reaction conditions. Furthermore, the large number of possible products highlights the rich chemistry of group 13 halides with dipyriddy ligands, which is coincidentally a problem to achieve phase-pure materials.

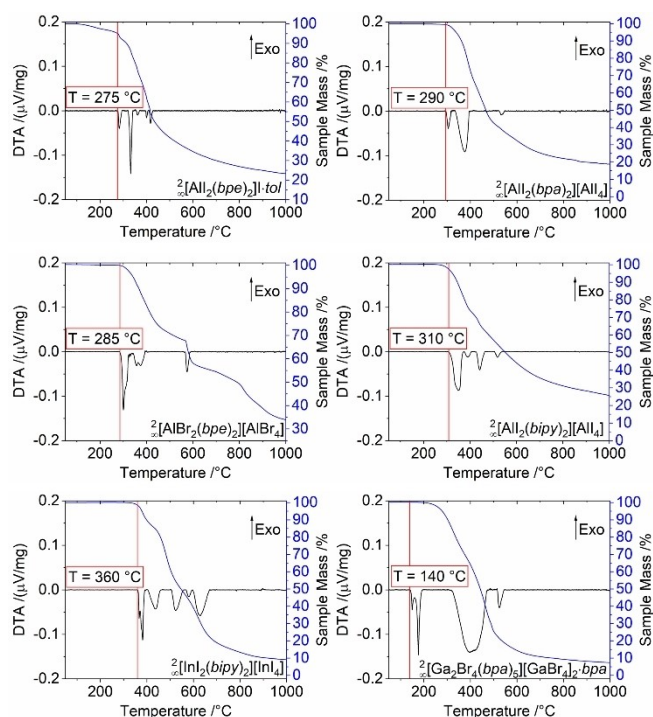


Figure 11. Simultaneous DTA/TG of **1** (Top, Left), **2** (Top, Right), **4** (Center, Left), **5** (Center, Right), **7** (Bottom, Left) and **8** (Bottom, Right). All measurements were performed in a constant argon flow of 50 mL min^{-1} with a heating rate of 5 K min^{-1} from room temperature to 1000°C .

Experimental Section

Synthesis and analytical data: The reactions of the group 13 metal halides AlBr₃, AlI₃, GaBr₃, InBr₃ and InI₃ with the bidentate dipyriddy ligands 1,2-di(4-pyridyl)ethylene (*bpe*), 1,2-di(4-pyridyl)ethane (*bpa*) and 4,4'-bipyridine (*bipy*) were carried out in sealed gas-over-pressure ampoules, with and without the use of solvents, such as toluene, *m*-xylene and even liquid naphthalene. All reactions make use of stoichiometric conditions and elevated temperatures and lead to various reaction products: ${}^2_{\infty}[\text{AlI}_2(\text{bpe})_2]\cdot\text{tol}$ (1), ${}^2_{\infty}[\text{AlI}_2(\text{bpa})_2][\text{AlI}_4]$ (2), ${}^2_{\infty}[\text{AlI}_2(\text{bpe})_2]\text{I}_3$ (3), ${}^2_{\infty}[\text{AlBr}_2(\text{bpe})_2][\text{AlBr}_4]$ (4), ${}^2_{\infty}[\text{AlI}_2(\text{bipy})_2][\text{AlI}_4]$ (5), ${}^2_{\infty}[\text{InBr}_2(\text{bipy})_2][\text{InBr}_4]$ (6), ${}^2_{\infty}[\text{InI}_2(\text{bipy})_2][\text{InI}_4]$ (7), ${}^2_{\infty}[(\text{GaBr}_2)_2(\text{bpa})_2][\text{GaBr}_4]_2\cdot\text{bpa}$ (8), ${}^1_{\infty}[\text{AlI}_2(\text{bpe})_3]\text{I}\cdot\text{bpe}$ (9), $[(\text{AlI}_2)_2(\text{bpe})_7]\text{I}_2\cdot(\text{Hbpe})\text{I}$ (10), $[(\text{AlBr}_3)_2(\text{bpe})]$ (11), $[(\text{AlI}_3)_2(\text{bpe})]$ (12), $[(\text{AlI}_3)_2(\text{bpa})]$ (13), $[(\text{GaBr}_3)_2(\text{bpa})]$ (14), $[(\text{AlI}_3)_2(\text{bipy})]\cdot 0.5\text{ tol}$ (15), $[(\text{GaBr}_3)_2(\text{bipy})]\cdot 0.5\text{ tol}$ (16). Detailed descriptions of the synthesis procedures for 1–16 can be found in the Supporting Information.

Deposition Number(s) 2073407 (1), 2073408 (2), 2120372 (3) and 2073409 (4), 2073410 (5), 2073411 (6), 2073412 (7), 2073413 (8), 2073414 (9), 2073415 (10), 2073416 (11), 2073417 (12), 2073418 (13), 2073419 (14), 2073420 (15), 2073421 (16) contain(s) the supplementary crystallographic data for this paper. These data are provided free of charge by the joint Cambridge Crystallographic Data Centre and Fachinformationszentrum Karlsruhe Access Structures service.

Details on crystallographic data, comparison of simulated and recorded powder XRD patterns, Pawley refinements, detailed IR bands from FTIR (ATR) investigations, thermal investigations as well as preparation details for all analysis procedures for compounds 1–16 can be found in the Supporting Information.

Acknowledgements

The authors gratefully acknowledge the Deutsche Forschungsgemeinschaft for supporting this work within the project MU-1562/7-2. Open Access funding enabled and organized by Projekt DEAL.

Conflict of Interest

The authors declare no conflict of interest.

Data Availability Statement

The data that support the findings of this study are available in the supplementary material of this article.

- [1] S. R. Batten, S. M. Neville, D. R. Turner, *Coordination Polymers. Design, Analysis and Application*, R. Soc. Chem., Cambridge 2009, 424.
- [2] C. Janiak, *Dalton Trans.* 2003, 14, 2781–2804.
- [3] C. Janiak, J. K. Vieth, *New J. Chem.* 2010, 34, 2366–2388.
- [4] S. Kitagawa, R. Matsuda, *Coord. Chem. Rev.* 2007, 251, 2490–2509.
- [5] S. R. Batten, N. R. Champness, X.-M. Chen, J. Garcia-Martinez, S. Kitagawa, L. Öhrström, M. O'Keeffe, M. Paik Suh, J. Reedijk, *Pure Appl. Chem.* 2013, 85, 1715–1724.
- [6] S. R. Batten, N. R. Champness, X.-M. Chen, J. Garcia-Martinez, S. Kitagawa, L. Öhrström, M. O'Keeffe, M. P. Suh, J. Reedijk, *CrystEngComm* 2012, 14, 3001–3004.
- [7] S. Bauer, N. Stock, *Chem. Unserer Zeit* 2008, 42, 12–19.

- [8] S. Kitagawa, R. Kitaura, S. Noro, *Angew. Chem. Int. Ed.* 2004, 43, 2334–2375; *Angew. Chem.* 2004, 116, 2388–2430.
- [9] J. Heine, K. Müller-Buschbaum, *Chem. Soc. Rev.* 2013, 42, 9232–9242.
- [10] C. Wang, T. Zhang, W. Lin, *Chem. Rev.* 2012, 112, 1084–1104.
- [11] M. Kurmoo, *Chem. Soc. Rev.* 2009, 38, 1353–1379.
- [12] J.-R. Li, J. Sculley, H.-C. Zhou, *Chem. Rev.* 2012, 112, 869–932.
- [13] W. Xie, Di Cui, S.-R. Zhang, Y.-H. Xu, D.-L. Jiang, *Mater. Horiz.* 2019, 6, 1571–1595.
- [14] J. Su, S. Yuan, H.-Y. Wang, L. Huang, J.-Y. Ge, E. Joseph, J. Qin, T. Cagin, J.-L. Zuo, H.-C. Zhou, *Nat. Commun.* 2017, 8, 2008.
- [15] G. Brunet, D. A. Safin, M. Z. Aghaji, K. Robeyns, I. Korobkov, T. K. Woo, M. Murugesu, *Chem. Sci.* 2017, 8, 3171–3177.
- [16] I. A. Baburin, V. A. Blatov, L. Carlucci, G. Ciani, D. M. Proserpio, *J. Solid State Chem.* 2005, 178, 2452–2474.
- [17] I. A. Baburin, V. A. Blatov, L. Carlucci, G. Ciani, D. M. Proserpio, *CrystEngComm* 2008, 10, 1822–1838.
- [18] S. R. Batten, R. Robson, *Angew. Chem. Int. Ed.* 1998, 37, 1460–1494; *Angew. Chem.* 1998, 110, 1558–1595.
- [19] W. L. Leong, J. J. Vittal, *Chem. Rev.* 2011, 111, 688–764.
- [20] D. M. Proserpio, *Nat. Chem.* 2010, 2, 435–436.
- [21] G.-P. Yang, L. Hou, X.-J. Luan, B. Wu, Y.-Y. Wang, *Chem. Soc. Rev.* 2012, 41, 6992–7000.
- [22] S.-Y. Zhang, Z. Zhang, M. J. Zaworotko, *Chem. Commun.* 2013, 49, 9700–9703.
- [23] V. A. Blatov, L. Carlucci, G. Ciani, D. M. Proserpio, *CrystEngComm* 2004, 6, 377–395.
- [24] L. Carlucci, G. Ciani, D. M. Proserpio, *Coord. Chem. Rev.* 2003, 246, 247–289.
- [25] Y.-N. Gong, D.-C. Zhong, T.-B. Lu, *CrystEngComm* 2016, 18, 2596–2606.
- [26] R. Haldar, N. Sikdar, T. K. Maji, *Mater. Today* 2015, 18, 97–116.
- [27] S. R. Batten, *CrystEngComm* 2001, 3, 67–72.
- [28] F. P. Gabbaï, A. Schier, J. Riede, *Angew. Chem. Int. Ed.* 1998, 37, 622–624; *Angew. Chem.* 1998, 110, 646–648.
- [29] N. Y. Gugin, A. Virovets, E. Peresypkina, E. I. Davydova, A. Y. Timoshkin, *CrystEngComm* 2020, 22, 4531–4543.
- [30] J. Heine, M. Holyńska, M. Reuter, B. Haas, S. Chatterjee, M. Koch, K. I. Gries, K. Volz, S. Dehnen, *Cryst. Growth Des.* 2013, 13, 1252–1259.
- [31] S. P. Petrosyants, *Russ. J. Inorg. Chem.* 2013, 58, 1605–1624.
- [32] S. P. Petrosyants, A. B. Ilyukhin, *Russ. J. Inorg. Chem.* 2010, 55, 30–33.
- [33] S. P. Petrosyants, A. B. Ilyukhin, *Russ. J. Inorg. Chem.* 2011, 56, 2047–2069.
- [34] C. R. Samanamú, A. F. Richards, *Polyhedron* 2007, 26, 923–928.
- [35] T. Schäfer, K. Müller-Buschbaum, *Z. Anorg. Allg. Chem.* 2018, 644, 1791–1795.
- [36] T. Schäfer, A. E. Sedykh, J. Becker, K. Müller-Buschbaum, *Z. Anorg. Allg. Chem.* 2020, 646, 1555–1562.
- [37] T. N. Sevastianova, E. I. Davydova, I. V. Kazakov, A. Y. Timoshkin, *Russ. Chem. Bull.* 2015, 64, 2523–2535.
- [38] T. N. Sevastianova, M. Bodensteiner, A. F. Maulieva, E. I. Davydova, A. V. Virovets, E. V. Peresypkina, G. Balázs, C. Graßl, M. Seidl, M. Scheer, G. Frenking, E. A. Berezovskaya, I. V. Kazakov, O. V. Khoroshilova, A. Y. Timoshkin, *Dalton Trans.* 2015, 44, 20648–20658.
- [39] J. R. Sorg, K. C. Oberst, K. Müller-Buschbaum, *Z. Anorg. Allg. Chem.* 2018, 644, 1293–1296.
- [40] J. R. Sorg, T. C. Schäfer, T. Schneider, K. Müller-Buschbaum, *Z. Anorg. Allg. Chem.* 2020, 646, 507–513.
- [41] J. R. Sorg, T. Schneider, L. Wohlfarth, T. C. Schäfer, A. Sedykh, K. Müller-Buschbaum, *Dalton Trans.* 2020, 49, 4904–4913.
- [42] J. R. Sorg, T. Wehner, P. R. Matthes, R. Sure, S. Grimme, J. Heine, K. Müller-Buschbaum, *Dalton Trans.* 2018, 47, 7669–7681.
- [43] J. Benecke, A. Fuß, T. A. Engesser, N. Stock, H. Reinsch, *Eur. J. Inorg. Chem.* 2021, 8, 713–719.
- [44] S. Halis, H. Reinsch, N. Stock, *Z. Anorg. Allg. Chem.* 2016, 642, 1340–1344.
- [45] T. Rhauderwiek, S. Waitschat, S. Wuttke, H. Reinsch, T. Bein, N. Stock, *Inorg. Chem.* 2016, 55, 5312–5319.
- [46] T. N. Sevastianova, M. Bodensteiner, A. S. Lisovenko, E. I. Davydova, M. Scheer, T. V. Susliakova, I. S. Krasnova, A. Y. Timoshkin, *Dalton Trans.* 2013, 42, 11589–11599.
- [47] P. A. Gale, J. W. Steed (Eds.) *Supramolecular Chemistry: From Molecules to Nanomaterials*, Vol. 6, Wiley 2012.
- [48] K. Biradha, A. Mondal, B. Moulton, M. J. Zaworotko, *Dalton Trans.* 2000, 21, 3837–3844.
- [49] H.-L. Jiang, T. A. Makal, H.-C. Zhou, *Coord. Chem. Rev.* 2013, 257, 2232–2249.

- [50] I. Krossing, H. Nöth, H. Schwenk-Kircher, T. Seifert, C. Tacke, *Eur. J. Inorg. Chem.* **1998**, 12, 1925–1930.
- [51] R. W. H. Small, I. J. Worrall, *Acta Crystallogr. Sect. B* **1982**, 38, 932–934.
- [52] J. A. J. Pardoe, A. R. Cowley, A. J. Downs, T. M. Greene, *Acta Crystallogr. Sect. C* **2005**, 61, m200–m202.
- [53] Q. Yu, X. Jiang, Z. Cheng, Y. Liao, M. Duan, *RSC Adv.* **2021**, 11, 30259–30269.
- [54] Z.-J. Li, Y. Ju, H. Lu, X. Wu, X. Yu, Y. Li, X. Wu, Z.-H. Zhang, J. Lin, Y. Qian, M.-Y. He, J.-Q. Wang, *Chem. Eur. J.* **2021**, 27, 1286–1291.
- [55] R.-X. Yao, X. Cui, X.-X. Jia, F.-Q. Zhang, X.-M. Zhang, *Inorg. Chem.* **2016**, 55, 9270–9275.
- [56] P. H. Svensson, L. Kloo, *Chem. Rev.* **2003**, 103, 1649–1684.
- [57] E. Cariati, D. Roberto, R. Ugo, P. C. Ford, S. Galli, A. Sironi, *Inorg. Chem.* **2005**, 44, 4077–4085.
- [58] B. Xin, G. Zeng, L. Gao, Y. Li, S. Xing, J. Hua, G. Li, Z. Shi, S. Feng, *Dalton Trans.* **2013**, 42, 7562–7568.
- [59] Z. Hu, B. J. Deibert, J. Li, *Chem. Soc. Rev.* **2014**, 43, 5815–5840.
- [60] J. Heine, T. Wehner, R. Bertermann, A. Steffen, K. Müller-Buschbaum, *Inorg. Chem.* **2014**, 53, 7197–7203.
- [61] R. I. Walton, *Chem. Soc. Rev.* **2002**, 31, 230–238.
- [62] A. Y. Timoshkin, A. V. Suvorov, A. D. Misharev, *Russ. J. Gen. Chem.* **2002**, 72, 1874–1877.

Manuscript received: November 19, 2021

Accepted manuscript online: February 18, 2022

Version of record online: March 18, 2022